remote sensing

MDPI

Article

Soil Moisture Estimation over Vegetated Agricultural Areas: Tigris Basin, Turkey from Radarsat-2 Data by Polarimetric Decomposition Models and a Generalized Regression Neural Network

Mehmet Siraç Özerdem [1], Emrullah Acar [2,*] and Remzi Ekinci [3]

1 Department of Electrical & Electronics Engineering, Faculty of Engineering, Dicle University, 21280 Diyarbakır, Turkey; sozerdem@dicle.edu.tr
2 Department of Electrical & Electronics Engineering, Faculty of Engineering and Architecture, Batman University, 72060 Batman, Turkey
3 Department of Field Crops, Faculty of Agriculture, Dicle University, 21280 Diyarbakır, Turkey; remzi.ekinci@dicle.edu.tr
* Correspondence: emrullah.acar@batman.edu.tr; Tel.: +90-541-462-1198

Academic Editors: Nicolas Baghdadi and Prasad S. Thenkabail
Received: 8 March 2017; Accepted: 19 April 2017; Published: 23 April 2017

Abstract: Determining the soil moisture in agricultural fields is a significant parameter to use irrigation systems efficiently. In contrast to standard soil moisture measurements, good results might be acquired in a shorter time over large areas by remote sensing tools. In order to estimate the soil moisture over vegetated agricultural areas, a relationship between Radarsat-2 data and measured ground soil moistures was established by polarimetric decomposition models and a generalized regression neural network (GRNN). The experiments were executed over two agricultural sites on the Tigris Basin, Turkey. The study consists of four phases. In the first stage, Radarsat-2 data were acquired on different dates and in situ measurements were implemented simultaneously. In the second phase, the Radarsat-2 data were pre-processed and the GPS coordinates of the soil sample points were imported to this data. Then the standard sigma backscattering coefficients with the Freeman–Durden and H/A/α polarimetric decomposition models were employed for feature extraction and a feature vector with four sigma backscattering coefficients (σhh, σhv, σvh, and σvv) and six polarimetric decomposition parameters (entropy, anisotropy, alpha angle, volume scattering, odd bounce, and double bounce) were generated for each pattern. In the last stage, GRNN was used to estimate the regional soil moisture with the aid of feature vectors. The results indicated that radar is a strong remote sensing tool for soil moisture estimation, with mean absolute errors around 2.31 vol %, 2.11 vol %, and 2.10 vol % for Datasets 1–3, respectively; and 2.46 vol %, 2.70 vol %, 7.09 vol %, and 5.70 vol % on Datasets 1 & 2, 2 & 3, 1 & 3, and 1 & 2 & 3, respectively.

Keywords: remote sensing; Radarsat-2; soil moisture; machine learning; GRNN; feature extraction; Freeman–Durden; H/A/α; polarimetric decomposition

1. Introduction

Soil moisture is commonly defined as the amount of water in the soil particles, and is a very important parameter in minimizing the harmful effects of drought, preventing salinity caused by overwatering, protecting agricultural land, and using irrigation systems efficiently [1]. Therefore, to determine the amount of water available in the soil used by plants, the soil moisture must be measured.

The retrieval of the soil moisture over large areas by gravimetric methods and digital probes is time-consuming, costly, and labor-intensive work [2]. However, successful results can be obtained in a shorter time by using remote sensing techniques. Thus, significant work has been done towards the application of active microwave sensors to monitoring soil surface moisture content [3]. Among the active microwave sensors, the Synthetic Aperture Radar (SAR) sensor plays an important role in agricultural monitoring, especially in plant growth, yield, mapping, and soil moisture estimation [4]. With the aid of polarimetric SAR, far better information can be derived than with single polarized SAR. The polarimetric SAR is less susceptible to weather conditions and capable of generating suitable high-resolution images for the purpose of agricultural soil monitoring. It provides information by multiple polarizations (hh, hv, vh, and vv) and penetrates the vegetative canopies [5]. Therefore, polarimetric SAR data can be used for soil moisture estimation over bare soil surface and vegetation-covered fields. In order to facilitate soil moisture estimation over vegetated agricultural areas, the contribution of the vegetation backscattering and ground scattering component must be separated from the observed backscattering [6]. Thus, polarimetric decomposition models are used to discretize the backscattering from the different layers by decomposing a scattering matrix (covariance matrix) into the linear combinations of some specific scattering mechanisms, like the odd bounce scattering, the even bounce scattering, and the volume scattering. The polarimetric decomposition models are based on two main approaches covering coherent decompositions and incoherent decompositions [7]. Among the decomposition techniques, $H/A/\alpha$, Freeman–Durden, Krogager, Touzi, and Yamaguchi are the most widely used models and various works have been done in the literature with the aid of these models. For example, Jagdhuber et al. [8] used the multi-angular polarimetric decomposition model for retrieving soil moisture and found a very high estimation rate with low RMSE (root mean square error). Hajnsek et al. [2] suggested a surface inversion model by using different model-based decompositions under vegetation cover. Xiaodong et al. [9] improved an adaptive two-component decomposition to estimate the soil moisture for C band Radarsat-2. In this study, the eigenvector-eigenvalue based ($H/A/\alpha$) and the model-based Freeman–Durden decomposition models were used for the feature extraction process since these models offer an efficient way to eliminate the effect of vegetation backscattering from the target backscattering in vegetated agricultural fields [10,11].

After the feature extraction process, a number of inversion models have been improved to estimate soil surface parameters from the texture features. The inversion models withstand three basic approaches in the literature, including the empirical/semi-empirical model [12–14], the theoretical model [10,15], and the machine learning model [4,16–20]. In the first approach, the empirical/semi empirical models are based on the scattering attitude of experimental measurements [16] and build a basic relationship between soil surface features and backscattering coefficients reflected from the target point [4]. Among the empirical models, Oh [12] and Dubois [13] are the most used inversion models. However, these models have a restricted range of practicability since they depend on site-specific surface parameters and empirical equations are inadequate to solve complex and nonlinear problems. Therefore, theoretical models are preferred as a second approach for soil moisture inversion due to their ability to consider situations that have not been regarded by the empirical models [16]. The Integral Equation Model (IEM) [15] is one of the most popular theoretical inversion models and can be used effectively over bare fields owing to its broad availability spectrum of surface roughness. However, this model is limited over vegetated areas since the vegetation causes complex volume backscattering. Moreover, the model requires some in situ measurements, such as surface morphology, which limits its applicability. Thus, the restraint of the model makes the inversions of such models highly complex and infeasible. To solve this problem, numerical inversion models such as machine learning must be considered as a third approach [18].

In machine learning models, soil surface moistures have been estimated successfully over bare and vegetated areas, and these models are used effectively in situations where both empirical and theoretical models are inadequate. Among the machine learning models, Support Vector Regression

(SVR) [4,6], Bayes Theorem [21], and Artificial Neural Network (ANN) [21–25] are commonly used inversion techniques for soil moisture retrieval. In the literature, a number of studies have been done using machine-learning-based inversion models. For instance, Weimann et al. [22] derived simulated data from the theoretical backscattering model over bare fields and used this data for training of ANN. They also improved the ANN training system by using remotely sensed ERS-2/ESAR data and observed low RMSE values between estimated soil moisture and ground soil moisture. Paloscia et al. [21] investigated the capabilities of the ENVISAT/ASAR data to provide soil moisture maps over agricultural areas. They compared the performances of three inversion algorithms including a feedforward neural network (ANN), a statistical Bayes' theorem, and the iterative Nelder–Mead method. The results indicated that the estimated data of the three methods were very close to the measured data and the accuracy of ANN was slightly higher than the other methods. Zhang et al. [4] investigated TerraSAR-X and Radarsat-2 data for soil moisture retrieval over bare agricultural areas using both statistical (SVR) and semi-empirical (Modified Dubois) approaches. Their results indicated that the TerraSAR-X and Radarsat-2 were proper remote sensing tools for soil moisture estimation with a low RMSE value. Notarnicola et al. [16] employed the ANN and statistical Bayesian methods for retrieving soil moisture from the active and passive data. The results showed that each method has similar performance, but the performance of the ANN was enhanced with increasing input number. Pasolli et al. [18] proposed two non-linear machine learning methods containing MLP Neural Network and SVR to estimate soil moisture from active and passive microwave data. The performance of these methods was then compared and the results showed that SVR was an alternative approach to MLP since it indicated better accuracy values in the case of limited samples. Said et al. [17] used ANN to retrieve the soil moisture over bare and vegetated surfaces with the aid of ERS-2 SAR data. The results showed a good correlation between the estimated and measured soil moisture. Moreover, ANN produced more precise results than multiple statistical regressions.

The purpose of this study is to determine a relationship between the fully polarimetric Radarsat-2 data and the ground soil moisture measurements as well as estimate the soil moisture over both vegetated and bare agricultural areas based on the determined relationship. The Radarsat-2 data were acquired on different dates in order to extract the sigma backscattering coefficients (σhh, σhv, σvh, and σvv), which describe the soil surface content. Furthermore, the H/A/α and Generalized Freeman–Durden methods were applied on fully polarimetric Radarsat-2 data and various backscattering parameters (entropy, anisotropy, alpha angle, volume scattering, surface scattering, and double bounce) and were derived for the feature extraction stage. After this step, GRNN was used to evaluate the potential of C-band SAR data for soil moisture inversion.

2. Materials

2.1. Study Area

The study area is located at the Tigris Basin in Diyarbakır province, Turkey (40°04′–40°26′ E, 37°46′–38°04′ N) and consists of two different agricultural lands that cover an average of 6 km^2 and 16 km^2 within the boundaries of the Dicle University campus (Figure 1). The mean slope of the study area is 3.05% and the mean elevation is 650 m. The average annual precipitation is approximately 496.0 mm/year and the average annual temperature is nearly 23.8 °C. This study area was dominated by cropland, which mostly includes wheat and barley during the period of SAR acquisitions (February 2015, April 2015, and June 2015). Hence, we concentrated on soil moisture estimation over vegetated agricultural areas.

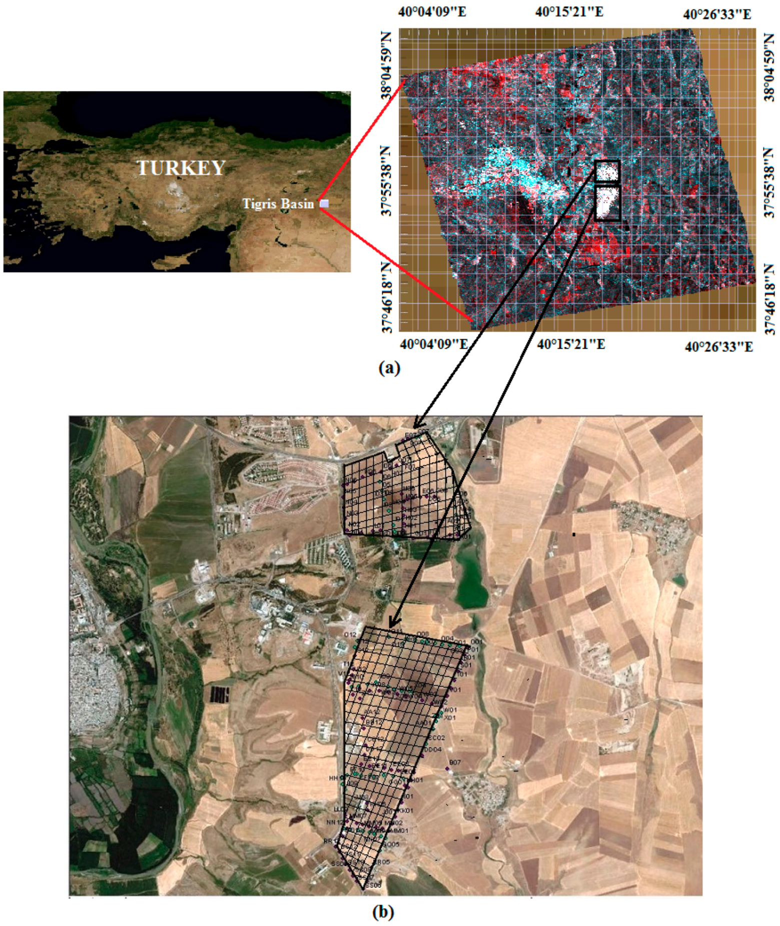

Figure 1. The location of the study area, presented as both (**a**) Radarsat-2 image and (**b**) Google Earth image. The black rectangular areas indicate the coverage of two experimental sites.

2.2. Ground Measurements

The ground measurements in the Tigris Basin were organized during 27 February, 8 April, and 10 June 2015 and carried out over two experimental areas at the same time as the Radarsat-2 acquisition. The experimental areas were divided into 100 × 100 m grids and soil surface samples were taken from at least one point of each grid, at 3–5 cm depth. An average of 300 ground soil samples were collected simultaneously with the Radarsat-2 transition for each period. These soil samples were then placed in 100 cm^3 metal cylinders and the location of each sample point was recorded with the help of a global positioning system (GPS). The distance between the sample points was nearly 100 m and the soil moisture content (SMC) for each sample was measured using gravimetric methods at the Dicle University Science and Application Research Center (DUBTAM). The gravimetrical soil moisture measurements (SM) for each period are given in Table 1.

Table 1. General information about gravimetrical soil moisture (%).

Measurement Period	Experimental Area	# Sample Points	Min SM	Max SM	Mean SM	SD of SM
27 February 2015	Sparsely Vegetated	335	18.76	43.6	29.72	4.76
8 April 2015	Densely Vegetated	285	20.24	41.37	30.36	3.93
10 June 2015	Bare	272	0.79	44.73	7.46	7.01

2.3. SAR Data Collection

In this study, the Radarsat-2 data was used over the experimental areas. Radarsat-2 is a world observation satellite that was successfully launched by the Canadian Space Agency in December 2007. It has a SAR sensor that runs at the C-band (5.33 GHz) of the microwave spectrum. Furthermore, it is fully polarimetric and provides multiple imaging modes [26]. In this study, three single-look complex (SLC) products that keep the resolution, phase, and amplitude information of the SAR data were used for estimating soil moistures [27]. Three Radarsat-2 data with Fine-Quad mode polarization were obtained during the different periods of product development. Each Radarsat-2 has a spatial resolution of 5.83 m and coverage of 30 km × 30 km.

2.4. Preprocessing of SAR Data

The preprocessing to be applied to the RADARSAT-2 data was performed in the following steps. Sentinel-1 Toolbox (S1TBX) [28] was used to read the SAR data and extract backscattering coefficients. The data were calibrated to correct SAR images radiometrically and a Refined Lee filter with 7 × 7 windows was used to remove the speckle noise. The filtered data were then geocoded using a SRTM-3 Digital Elevation Model (DEM) and Geographical Latitude/Longitude (WGS84) was chosen as the default output map projection. The GPS values of the sample points were converted to shp-extended vectors by ARCGIS 10.2, then imported to the Radarsat-2 data with the aid of the Sentinel-I toolbox. The accurate geographical registration among the field measurements and Radarsat-2 data was accomplished by utilizing the corner reflectors in the study area. The preprocessed Radarsat-2 images are shown in Figure 2.

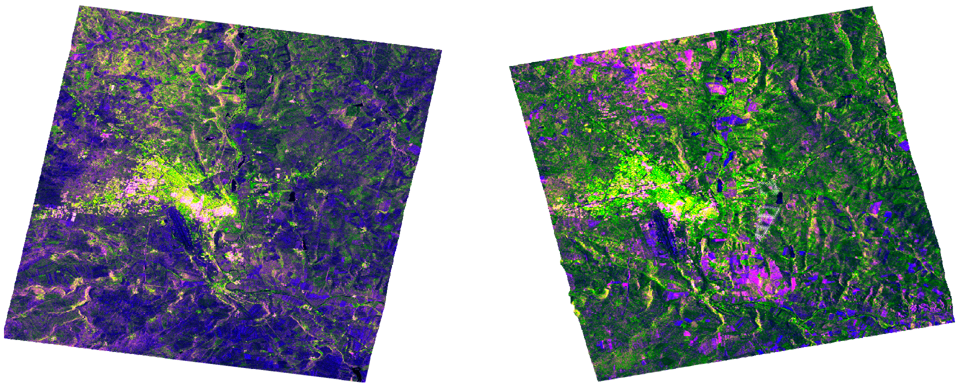

(**a**) (**b**)

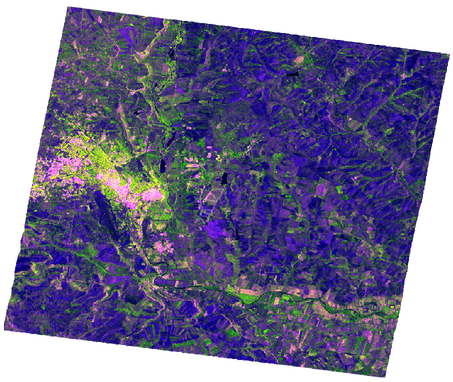

(**c**)

Figure 2. Three Radarsat-2 images were acquired over the Tigris Basin, Diyarbakır and preprocessed on (**a**) 27 February 2015; (**b**) 8 April 2015; and (**c**) 10 June 2015. The Dual pol (hh + vv) RGB image was obtained by combining three different (R = hh; G = vh; B = hh/hv) bands of Radarsat-2 data.

3. Methods

3.1. Feature Extraction from SAR Data

After the pre-processing step, each GPS value of the sampling point, which corresponds to a SAR pixel, was represented by a cell (3 × 3 pixels) using a 3 × 3 window. These cells are different patterns of the training set and the backscattering coefficients of these patterns were calculated by taking the average of the coefficients in the cell. In order to form a feature vector for each pattern, three feature extraction models were used in this study. In the first approach, four sigma backscattering coefficients (σhh, σhv, σvh, and σvv) were derived from the patterns of different bands (hh, hv, vh, and vv) using standard SAR backscattering coefficients. In the second approach, six backscattering coefficients in total were extracted by using the Freeman–Durden (odd bounce, even bounce, and volume scattering) and H/A/α (entropy, anisotropy, and alpha angle) decomposition models.

3.1.1. Freeman–Durden Decomposition Model

The Freeman–Durden decomposition model is based on three independent scattering mechanisms including volume scattering, double bounce, and odd bounce, and they can be interpreted physically [29]. Figure 3 shows the scattering mechanisms.

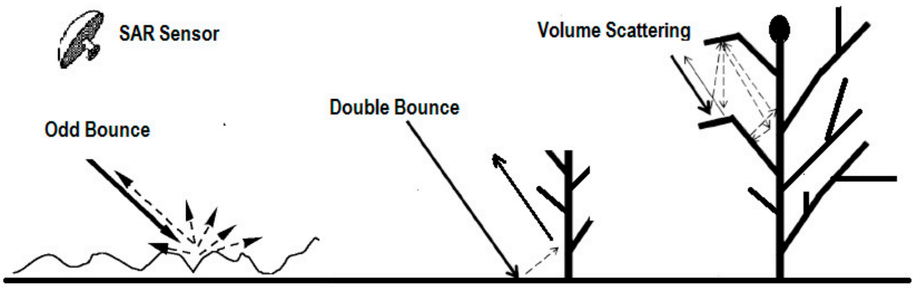

Figure 3. Three surface scattering mechanisms.

Among these components, the volume scattering expresses the canopy scattering generated by randomly oriented dipole clouds. It is supposed that the radar signal is backscattered from a cloud of randomly oriented scatterers, which are very thin and cylinder-like. In order to simulate such scatterers, it is assumed that an elementary dipole is oriented horizontally in the perpendicular linear x–y plane. Let the volume scattering be symbolized by the scatterers, which are in standard orientation, as shown in the scattering matrix in Equation (1) [29]:

$$S_{2X2,dipole} = \begin{pmatrix} S_V & 0 \\ 0 & S_H \end{pmatrix}, \quad S_V >> S_H \quad . \tag{1}$$

In this equation, S_V and S_H denote complex scattering coefficients and they are considered $S_V >> S_H$ since the dipole is oriented horizontally. If a dipole is turning around the radar look direction under the θ angle, the scattering matrix of the oriented dipole (scatterer) is as in Equation (2):

$$S_\vartheta = \begin{bmatrix} Svv & S_{HV} \\ S_{VH} & S_{HH} \end{bmatrix} = \begin{bmatrix} S_V Cos^2(\theta) + S_H Sin^2(\theta) & (S_V - S_H)Cos(\theta)Sin(\theta) \\ (S_V - S_H)Cos(\theta)Sin(\theta) & S_H Cos^2(\theta) + S_V Sin^2(\theta) \end{bmatrix}. \tag{2}$$

Since the radar transmitter and receiver coordinate systems are the same, the created scattering matrix becomes symmetric; thus, S_{HV} and S_{VH} are considered equal. Scatterers (dipoles) can be randomly directed by the $p(\theta)$ probability density function (PDF) in the radar look direction. The expected value of any function $f(\theta)$ is given by Equation (3):

$$\langle f \rangle = \int_0^{2\pi} f(\vartheta)p(\vartheta)d\vartheta. \tag{3}$$

The covariance matrix for volume (canopy) scattering is represented in Equation (4) and the matrix elements are generated using Equation (3):

$$C_{3X3} = S * S^{T*} = \begin{pmatrix} S_{HH}S^*{}_{HH} & \sqrt{2}S_{HH}S^*{}_{HV} & S_{HH}S^*{}_{VV} \\ \sqrt{2}S_{HV}S^*{}_{HH} & 2S_{HV}S^*{}_{HV} & \sqrt{2}S_{HV}S^*{}_{VV} \\ S_{VV}S^*{}_{HH} & \sqrt{2}S_{VV}S^*{}_{HV} & S_{VV}S^*{}_{VV} \end{pmatrix}. \tag{4}$$

In order to simplify the equations, the uniformly distributed probability function is assumed to be $p(\theta) = 1$ and the thin cylindrical scatterers are $S_V = 1$ and $S_H = 0$. Thus situated, the covariance matrix for volume (canopy) scatter is expressed in Equation (7) using the parameters of Equations (5) and (6):

$$\langle S_{HH}S*_{HH} \rangle = \left\langle S_{HH}{}^2 \right\rangle = \left\langle S_{VV}{}^2 \right\rangle = 1,\ \langle S_{HH}S*_{VV} \rangle = \left\langle S_{HV}{}^2 \right\rangle = 1/3 \tag{5}$$

$$\langle S_{HH}S*_{HV} \rangle = \langle S_{HV}S*_{VV} \rangle = 0 \tag{6}$$

$$\langle C_{3,vol} \rangle = \begin{pmatrix} S_{HH}S^*{}_{HH} & \sqrt{2}S_{HH}S^*{}_{HV} & S_{HH}S^*{}_{VV} \\ \sqrt{2}S_{HV}S^*{}_{HH} & 2S_{HV}S^*{}_{HV} & \sqrt{2}S_{HV}S^*{}_{VV} \\ S_{VV}S^*{}_{HH} & \sqrt{2}S_{VV}S^*{}_{HV} & S_{VV}S^*{}_{VV} \end{pmatrix} = \frac{f_V}{3} \begin{pmatrix} 3 & 0 & 1 \\ 0 & 2 & 0 \\ 1 & 0 & 3 \end{pmatrix}. \tag{7}$$

Here, f_v represents the effect of volume scattering on the $|\mathrm{Svv}|^2$ factor.

The double bounce scattering is the second component of the Freeman–Durden decomposition, in which a dihedral corner reflector is used to model the scattering stage. For example, the surfaces of a tree trunk and the ground can be used as a dihedral reflector. The covariance matrix for this component is described in Equation (10) using Equations (8) and (9) [29]:

$$\langle S_{HH}S*_{HH} \rangle = \left\langle S_{HH}{}^2 \right\rangle = |\alpha|^2,\ \left\langle S_{VV}{}^2 \right\rangle = 1,\ \langle S_{HH}S*_{VV} \rangle = \alpha,\ \left\langle S_{HV}{}^2 \right\rangle = 0 \tag{8}$$

$$\langle S_{HH}S*_{HV} \rangle = \langle S_{HV}S*_{VV} \rangle = 0 \tag{9}$$

$$\langle C_{3,db} \rangle = \begin{pmatrix} S_{HH}S^*{}_{HH} & \sqrt{2}S_{HH}S^*{}_{HV} & S_{HH}S^*{}_{VV} \\ \sqrt{2}S_{HV}S^*{}_{HH} & 2S_{HV}S^*{}_{HV} & \sqrt{2}S_{HV}S^*{}_{VV} \\ S_{VV}S^*{}_{HH} & \sqrt{2}S_{VV}S^*{}_{HV} & S_{VV}S^*{}_{VV} \end{pmatrix} = f_d \begin{pmatrix} |\alpha|^2 & 0 & \alpha \\ 0 & 0 & 0 \\ \alpha* & 0 & 1 \end{pmatrix}, \tag{10}$$

where f_d indicates the contribution of the double bounce scattering to the $|\mathrm{Svv}|^2$ factor. Lastly, the odd bounce scattering refers to the backscattering from a rough surface and a first-order Bragg surface scattering model is used to represent the rough surfaces in this mechanism. The covariance matrix for this component is described in Equation (13) with the aid of Equations (11) and (12) [29]:

$$\langle S_{HH}S*_{HH} \rangle = \left\langle S_{HH}{}^2 \right\rangle = |\beta|^2,\ \left\langle S_{VV}{}^2 \right\rangle = 1,\ \langle S_{HH}S*_{VV} \rangle = \beta,\ \left\langle S_{HV}{}^2 \right\rangle = 0 \tag{11}$$

$$\langle S_{HH}S*_{HV} \rangle = \langle S_{HV}S*_{VV} \rangle = 0 \tag{12}$$

$$\langle C_{3,sur} \rangle = \begin{pmatrix} S_{HH}S^*{}_{HH} & \sqrt{2}S_{HH}S^*{}_{HV} & S_{HH}S^*{}_{VV} \\ \sqrt{2}S_{HV}S^*{}_{HH} & 2S_{HV}S^*{}_{HV} & \sqrt{2}S_{HV}S^*{}_{VV} \\ S_{VV}S^*{}_{HH} & \sqrt{2}S_{VV}S^*{}_{HV} & S_{VV}S^*{}_{VV} \end{pmatrix} = f_s \begin{pmatrix} |\beta|^2 & 0 & \beta \\ 0 & 0 & 0 \\ \beta* & 0 & 1 \end{pmatrix}, \tag{13}$$

where f_s shows the contribution of surface scattering to the $|Svv|^2$ factor. On account of this, the measured covariance matrix of the Freeman–Durden decomposition can be defined as the summation of three covariance scattering matrices, as shown in Equation (14) [29]:

$$\langle C_3 \rangle = \langle C_{3,vol} \rangle + \langle C_{3,db} \rangle + \langle C_{3,sur} \rangle. \tag{14}$$

3.1.2. H/A/α Decomposition Model

The H/A/α decomposition model is built on the eigenvalue and eigenvector analysis of the coherency matrix T_3, which is expressed as in Equation (15) [30]:

$$\langle T_3 \rangle = \frac{1}{2}\begin{pmatrix} \left\langle |S_{HH}+S_{VV}|^2 \right\rangle & \langle (S_{HH}+S_{VV})(S_{HH}-S_{VV})^* \rangle & \langle 2S^*{}_{HV}(S_{HH}+S_{VV}) \rangle \\ \langle (S_{HH}-S_{VV})(S_{HH}+S_{VV})^* \rangle & \left\langle |S_{HH}-S_{VV}|^2 \right\rangle & \langle 2S^*{}_{HV}(S_{HH}-S_{VV}) \rangle \\ \langle 2S_{HV}(S_{HH}+S_{VV})^* \rangle & \langle 2S_{HV}(S_{HH}-S_{VV})^* \rangle & \left\langle 4|S_{HV}|^2 \right\rangle \end{pmatrix}, \tag{15}$$

where the coherency matrix T_3 is represented in Equation (16):

$$\langle T_3 \rangle = u_3 \lambda u_3{}^{-1}, \quad \lambda = \begin{bmatrix} \lambda_1 & 0 & 0 \\ 0 & \lambda_2 & 0 \\ 0 & 0 & \lambda_3 \end{bmatrix}. \tag{16}$$

Here, the λ matrix consists of the eigenvalues computed from T_3. Additionally, the calculated eigenvectors u_i are shown in Equation (17):

$$u_i = \begin{bmatrix} \cos\alpha_i \\ \sin\alpha_i \cos\beta_i e^{j\delta_i} \\ \sin\alpha_i \cos\beta_i e^{j\gamma_i} \end{bmatrix}. \tag{17}$$

Three eigenvectors (for i = 1, 2, 3) are then used to form the u_3 unitary matrix, as shown in Equation (18):

$$u_3 = [u_1\, u_2\, u_3] = \begin{bmatrix} \cos\alpha_1 & \cos\alpha_2 & \cos\alpha_3 \\ \sin\alpha_1\cos\beta_1 e^{j\delta_1} & \sin\alpha_2\cos\beta_2 e^{j\delta_2} & \sin\alpha_3\cos\beta_3 e^{j\delta_3} \\ \sin\alpha_1\cos\beta_1 e^{j\gamma_1} & \sin\alpha_2\cos\beta_2 e^{j\gamma_2} & \sin\alpha_3\cos\beta_3 e^{j\gamma_3} \end{bmatrix}, \tag{18}$$

where α is the incidence angle, β is the orientation angle, and γ and δ explain the relation of phases. One of the most important aspects of this decomposition model is that the parameters are invariant and constant for rotation around the radar line. Thus, three statistical features including polarimetric entropy (H), anisotropy (A), and alpha angle (α) have been described to make the analysis of this model easier, as shown in Equations (19)–(21), respectively [30]:

$$H = -\sum_{i=1}^{3} P_i \log_3(P_i), \quad P_i = \frac{\lambda_i}{\sum_{r=1}^{3} \lambda_r}, \quad 0 \le H \le 1 \tag{19}$$

$$A = \frac{\lambda_2 + \lambda_3}{\lambda_2 - \lambda_3}, \quad 0 \le A \le 1 \tag{20}$$

$$\widehat{\alpha} = \sum_{i=1}^{3} P_i \alpha_i, \quad 0 \le \widehat{\alpha} \le \frac{\pi}{2}. \tag{21}$$

Here, P_i represents the probability of each eigenvalue λ_i.

3.2. GRNN Algorithm

The Generalized Regression Neural Network (GRNN) is a strong and nonlinear machine learning technique and it has the ability to retrieve complex, dynamic, and non-linear patterns from the data [31,32]. It was used to estimate the soil moisture by way of a relationship between measured ground soil moisture and the backscattering coefficient. GRNN has input, pattern, summation, and output layers. The pattern and summation layers can be named hidden layers because they are inside the neural network and do not have any contact with the external surroundings.

The architecture of the GRNN model is indicated in Figure 4. Ten neurons corresponding to different backscattering parameters (σhh, σhv, σvh, σvv, entropy, anisotropy, alpha angle, volume scattering, surface scattering, and double bounce) are used in the input layer. Moreover, the pattern layer is attached to the input layer and the neurons of the pattern layer indicate training patterns. The nonlinear analysis of the input data is implemented in this layer and the distance between input and sample data is measured as the output data of the pattern layer. Then, all neurons of the pattern layer are connected to the summation layer, which has two types of summation neurons (one neuron and multiple neurons). The summation neurons are used to sum the weighted and unweighted outputs of the neurons in the pattern layer. Finally, the one neuron of the output layer computes the outputs of the summation layer to give the estimated result.

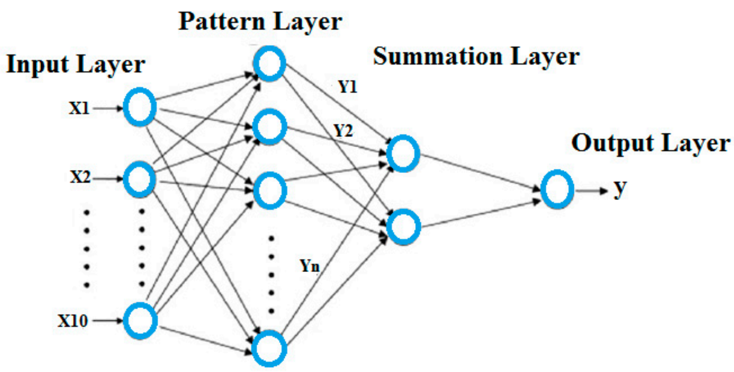

Figure 4. The architecture of the GRNN model.

Assume that x and y become input and output variables, as seen in Equations (22) and (23), respectively:

$$x = [x_1, x_2 ... x_m]^T \tag{22}$$

$$y = [y_1, y_2 ... y_n]^T. \tag{23}$$

The target parameter y can be estimated from x variables by the GRNN regression model. Therefore, the estimated y can be computed as shown in Equation (24) [31]:

$$\hat{y}(x) = \frac{\sum_{i=1}^{n} y^i \exp\left(-\frac{C_i}{\varsigma}\right)}{\sum_{i=1}^{n} \exp\left(-\frac{C_i}{\varsigma}\right)}, \quad C_i = \sum_{j=1}^{p} \left| x_j - x_j^i \right| \tag{24}$$

Where n and ς indicate the number of training samples and the spread parameter, respectively. The spread parameter is an important parameter to affect the accuracy of the GRNN model and is used to arrange the kernel width of the Gaussian function [33].

4. Results

This section explains the results obtained from the standard sigma backscattering coefficients and polarimetric decomposition models. A nonlinear machine learning regression model was trained and tested on the basis of scattering components to estimate soil moisture content. Three datasets were generated in a new manner and the analysis of these datasets is shown below.

4.1. Experiments on Dataset 1

In this phase, Dataset 1 was constituted from Radarsat-2 data of 27 February 2015 in order to evaluate the impact of low vegetation cover over the study areas and the following steps were implemented to form Dataset 1. First of all, the standard sigma backscattering technique was applied to the Radarsat-2 data and four sigma backscattering coefficients were computed for each sampling cell. Then, Freeman–Durden and H/A/α decomposition models were employed and three physical three statistical parameters were extracted from the sampling cells. To process the fully polarimetric Radarsat-2 data, calibration, polarimetric matrix generation (generally T_3 Coherency matrix), polarimetric speckle filtering (typically Refined Lee Filter), and polarimetric decompositions steps are mandatory. The images that resulted after data processing are shown in Figure 5.

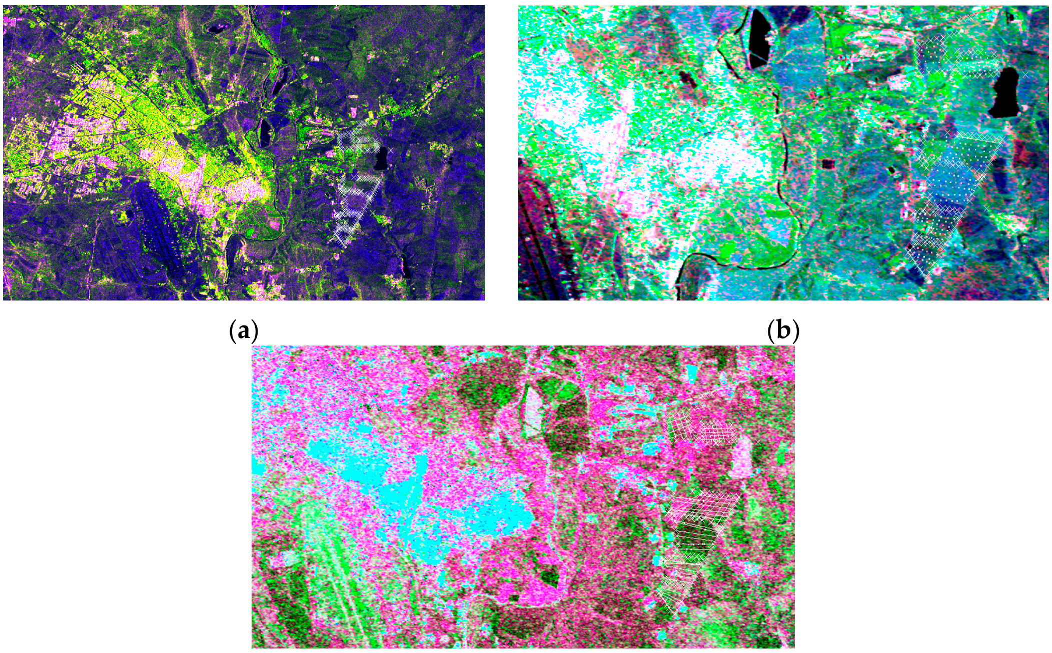

(**a**) (**b**) (**c**)

Figure 5. The resulting Radarsat-2 data from 27 February 2015 after (**a**) standard sigma backscattering technique; (**b**) Freeman–Durden; and (**c**) H/A/α models.

The extracted parameters were then added in succession and the feature vector of 10 units in length (σhh, σhv, σvh, σvv, entropy, anisotropy, alpha angle, volume scattering, surface scattering, and double bounce) was generated from each sampling point. This process was repeated for 335 sampling points in this period and Dataset 1 with 335 × 10 lengths was formed.

In order to correlate the ground measurement data with the generated feature vectors as well as estimate the moisture value of sampling points not included in the calculation, GRNN was used as an inversion model. For computing the accuracy of the system, training and test sets were established from Dataset 1 and the moisture values of the agricultural areas included in the test set were estimated by the trained GRNN. Moreover, the spread parameter (ς) was set in the range (0.5–1.5) and was chosen as ς = 1 in this study since it provides the best performance at this value for all GRNN models.

In order to determine the effect of the spread parameter, the result of one application example was shown in Table 2.

Table 2. The effect of spread parameter on GRNN for testing Dataset 1.

Spread Parameter (ς)	R	RMSE (%)	MAE (%)
0.5	0.73	3.47	2.66
0.6	0.78	3.04	2.50
0.7	0.79	2.93	2.41
0.8	0.80	2.86	2.35
0.9	0.80	2.85	2.32
1.0	0.80	2.84	2.31
1.1	0.80	2.88	2.35
1.2	0.79	2.93	2.39
1.3	0.78	2.99	2.43
1.4	0.77	3.05	2.48
1.5	0.76	3.12	2.52

In the testing process, the leave-one-out cross validation method was used to validate the overall system accuracy and each of the patterns forming Dataset 1 was included in the test set alternately. Thus, the quantitative evaluation between measured and estimated soil moistures was determined by GRNN, as shown in Figure 6.

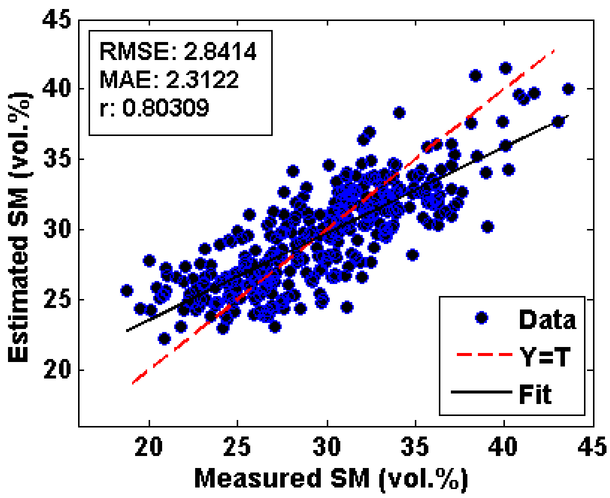

Figure 6. The relationship between the measured and estimated soil moistures (SM) for Dataset 1.

For the performance analysis, Root Mean Square Error (RMSE), Correlation Coefficient (r), and Mean Absolute Error (MAE) were chosen as the indicators. After a leave-one-out cross-validation process, the overall system accuracy was observed with the estimation error of around 2.84 vol % RMSE and 2.31 vol % MAE for Dataset 1.

On the other hand, four test areas (22 sampling points for each test area) were randomly selected on the basis of the Monte Carlo cross-validation method to validate the precision of the system over the local regions. Finally, the results (see Figure 7) showed estimation errors of 2.80 vol %, 2.79 vol %, 2.70 vol %, and 2.55 vol % MAE over testing areas 1–4, respectively.

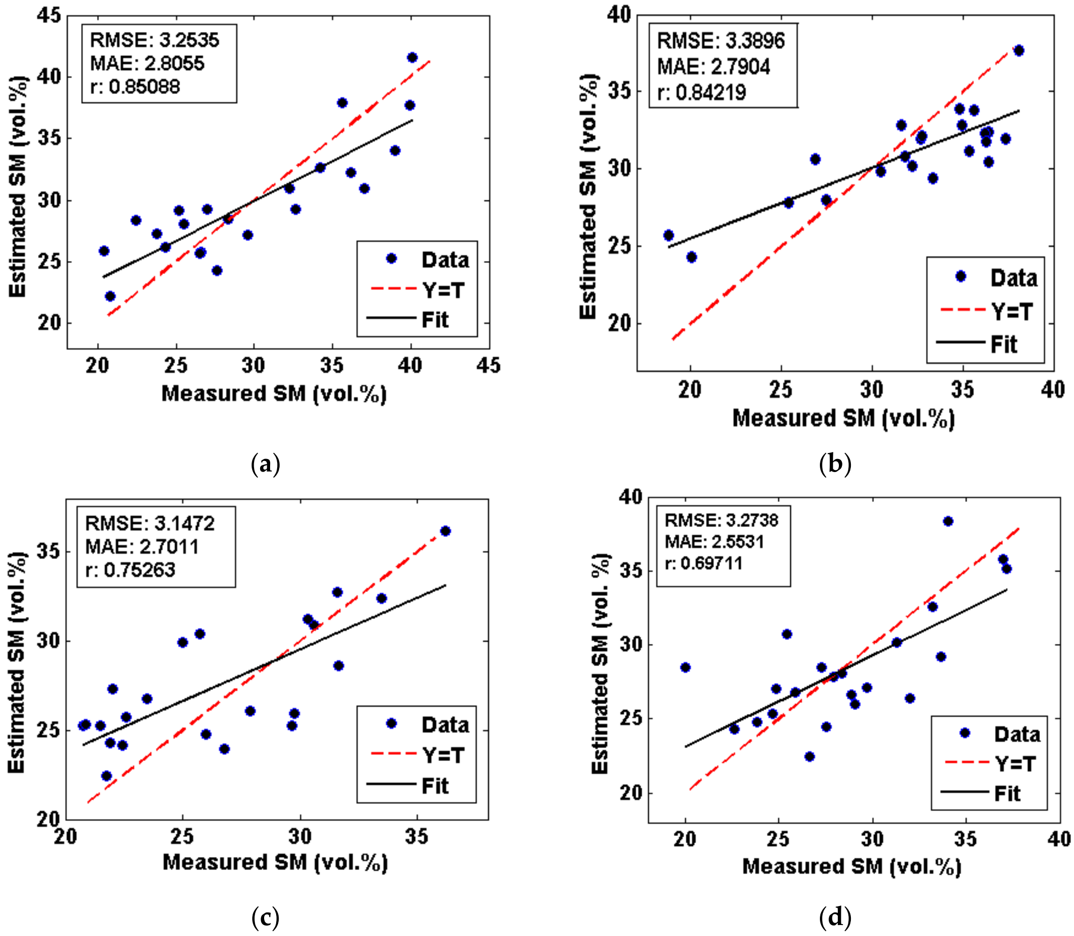

Figure 7. The relationship between the measured and estimated soil moistures (SM) over testing areas 1–4 for Dataset 1 (**a**–**d**), respectively.

4.2. Experiments on Dataset 2

For this stage, Dataset 2 was created from Radarsat-2 data of 8 April 2015 to analyze the effect of dense vegetation cover over the study areas. The same topology used in Section 4.1 was repeated in this stage to estimate soil moisture and then Dataset 2 with 285 × 10 lengths was generated. After the Radarsat-2 processing step, the resulting images are presented in Figure 8 In order to validate the applicability of the overall system, the leave-one-out cross-validation method was implemented in the testing stage, resulting in estimation errors of 2.65 vol % RMSE and 2.11 vol % MAE over the two experimental areas, as described in Figure 9. Moreover, the four test areas (25 sampling points for each test area) were randomly chosen for validation of local regions and their accuracy results are given in Figure 10. The experimental results indicated that the MAE was 2.78 vol %, 1.79 vol %, 2.61 vol %, and 1.98 vol % over test areas 1–4, respectively.

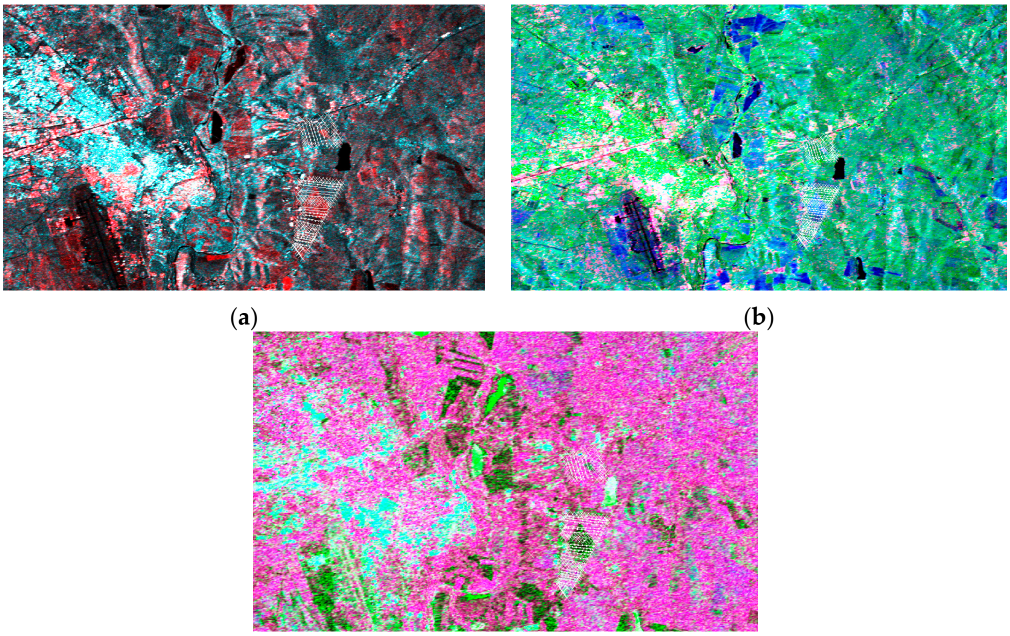

(**a**) (**b**)

(**c**)

Figure 8. Radarsat-2 data from 8 April 2015 after (**a**) standard sigma backscattering technique; (**b**) Freeman–Durden; and (**c**) H/A/α models.

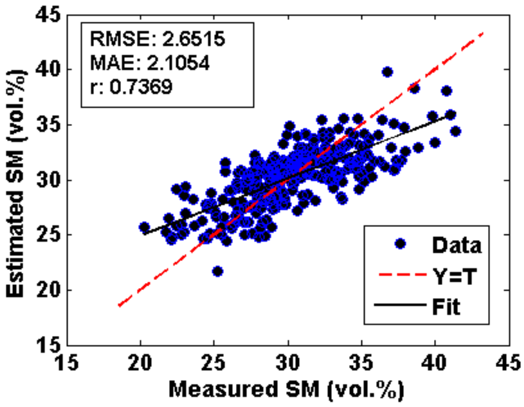

Figure 9. The relationship between measured and estimated SM for Dataset 2.

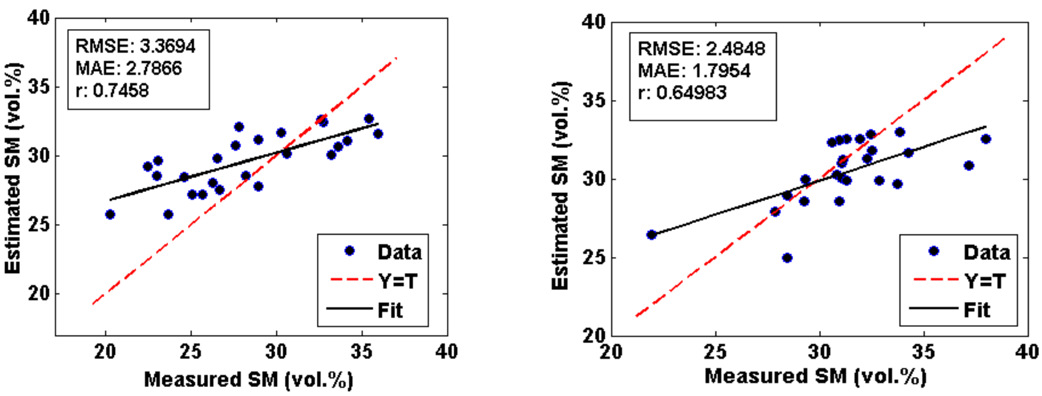

(**a**) (**b**)

Figure 10. *Cont.*

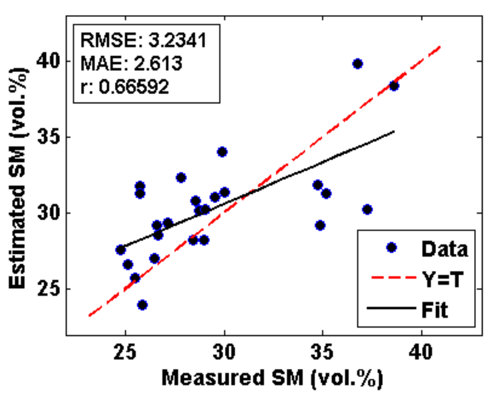

(**c**)

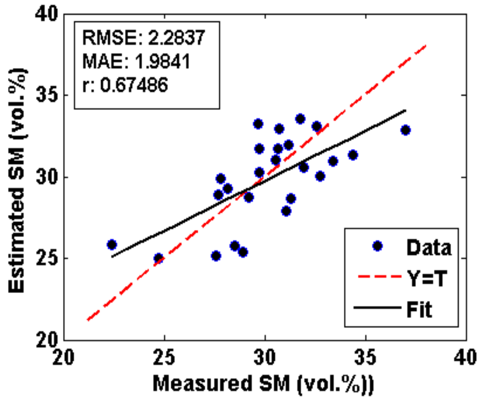

(**d**)

Figure 10. The relationship between measured and estimated SM over testing areas 1–4 for Dataset 2 (**a**–**d**), respectively.

4.3. Experiments on Dataset 3

In this period, Dataset 3 was generated from the Radarsat-2 data of 10 June 2015 for estimating the soil moisture over bare agricultural areas. A similar approach to that in the Sections 4.1 and 4.2 was employed for this phase and Dataset 3 with 272 × 10 lengths was constructed. After the decomposition process, we obtained the results shown in Figure 11. The overall system accuracy for this period was calculated with estimation error of 2.77 vol % RMSE and 2.10 vol % MAE, as displayed in Figure 12. Furthermore, four test regions (25 sampling points for each test area) were picked out randomly and the precision values of these sites are represented in Figure 13. Eventually, MAE of 2.10 vol % and 2.55 vol % was computed for test areas 1–2, respectively, with 2.11 vol % and 3.05 vol % for test areas 3–4, respectively.

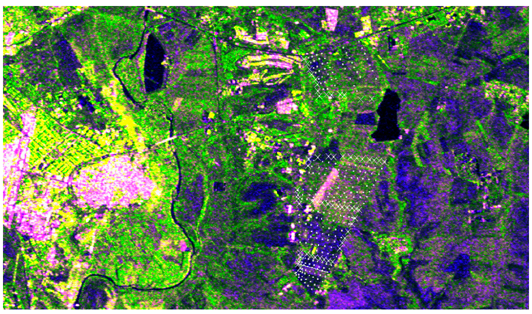

(**a**)

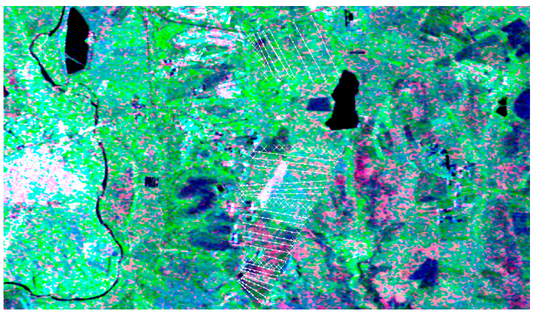

(**b**)

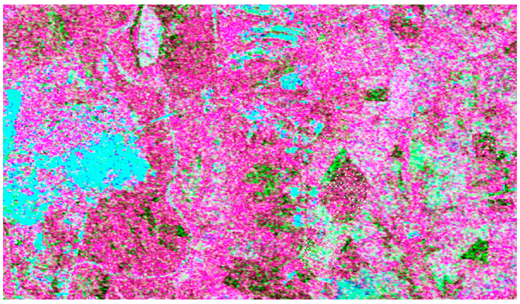

(**c**)

Figure 11. Radarsat-2 data from derived 10 June 2015 after (**a**) standard sigma backscattering technique; (**b**) Freeman–Durden; and (**c**) H/A/α models.

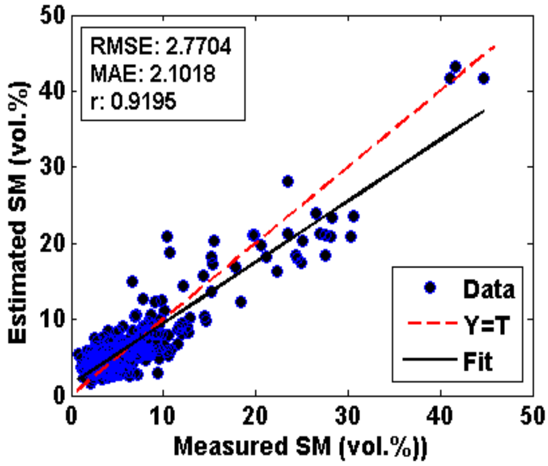

Figure 12. The relationship between measured and estimated SM for Dataset 3.

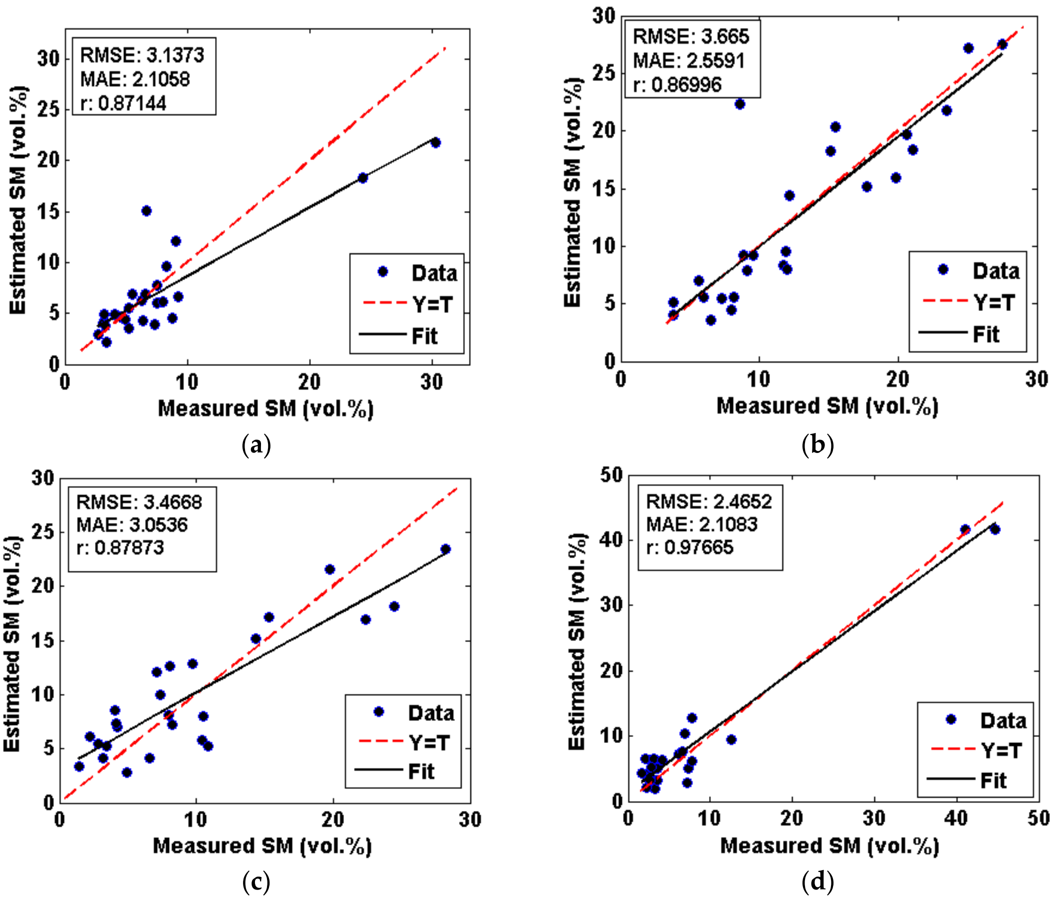

Figure 13. The relationship between measured and estimated SM over testing areas 1–4 for Dataset 3 (**a**–**d**), respectively.

4.4. Experiments on Combined Datasets

In order to prove the applicability and usefulness of the proposed algorithm for soil moisture estimation on different dates, the obtained datasets were merged in the following approaches. In the first instance, Datasets 1&2 were combined to determine the effect of low and dense vegetation cover at different dates and a new dataset with 620 $\times$ 10 lengths was formed. Then, the GRNN algorithm was used for soil moisture estimation on the basis of combined datasets. In the testing stage, the leave-one-out cross-validation method was employed to test the overall system performance. Consequently, estimation errors of 3.23 vol % RMSE and 2.46 vol % MAE were computed, as displayed in Figure 14.

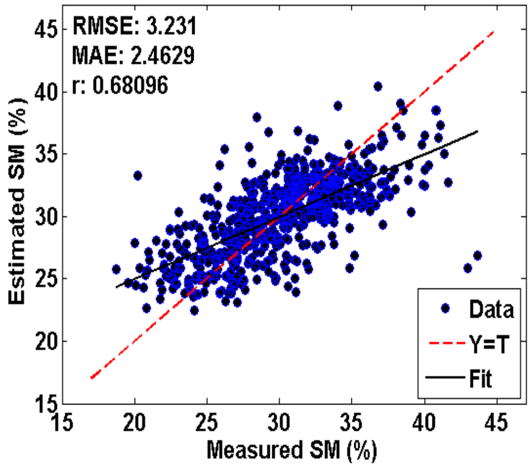

Figure 14. The relationship between measured and estimated SM for combined Datasets 1&2.

In the second approach, Datasets 1&3 were combined to analyze the influence of low vegetation and bare soil surface on different dates and a dataset with 607 × 10 lengths was generated. After the training and testing process, the quantitative comparison between measured and estimated soil moistures (as indicated in Figure 15) was 9.76 vol % RMSE and 7.09 vol % MAE.

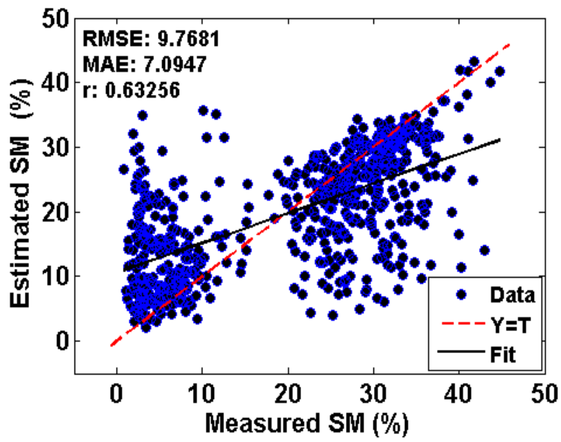

Figure 15. The relationship between measured and estimated SM for combined Datasets 1&3.

In the next approach, Datasets 2&3 were combined to determine the effect of dense vegetation and bare soil surface on different dates and a dataset with 557 × 10 lengths was formed. The same topology as in the first approach was used in this stage for the validation and testing of the proposed model; the relationship between measured and estimated soil moistures is displayed in Figure 16. Consequently, estimation errors of 4.04 vol % RMSE and 2.69 vol % MAE were computed for this scenario.

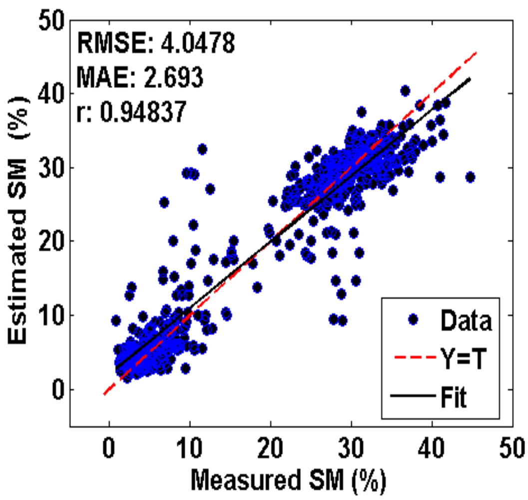

Figure 16. The relationship between measured and estimated SM for combined Datasets 2&3.

Finally, Datasets 1&2&3 were merged to examine the influence of low vegetation, dense vegetation, and bare soil surface on different dates and a dataset with 892×10 lengths was constituted. After the validation and testing process, the quantitative comparison between the measured and generated data (Figure 17) was shown to be 8.25 vol % RMSE and 5.69 vol % MAE.

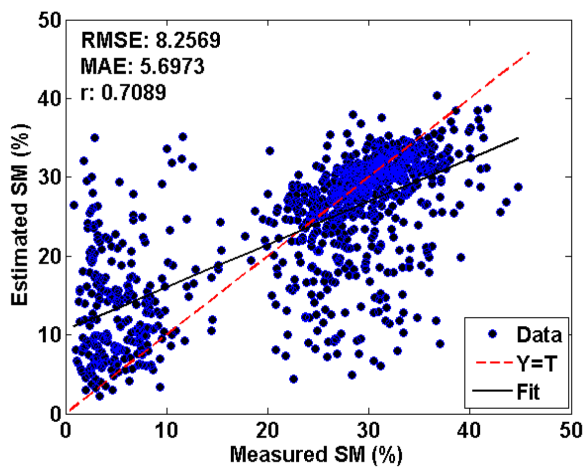

Figure 17. The relationship between measured and estimated SM for combined Datasets 1&2&3.

5. Discussion

There are a small number of research studies estimating the soil moisture by polarimetric decomposition models and nonlinear machine learning techniques. In this study, two typical polarimetric decomposition models (Freeman–Durden, $H/A/\alpha$) were picked out to obtain the different scattering components at different vegetation growth stages. The Freeman–Durden decomposition model was used in this study since it does not need any ground measurements like surface parameters. Moreover, the $H/A/\alpha$ method was employed as a second decomposition model because it covers all possible scenarios of scattering models, especially surface scattering. The regression analysis of the datasets was then implemented using the GRNN algorithm. In order to evaluate the results of three datasets, the statistical relationship between the measured and estimated soil moistures is given in Table 3 with a new parameter: coefficient of variation (C_V).

Table 3. The statistical relationship between measured and estimated soil moistures (SM).

Experimental Dataset	Average SM (%)	RMSE (%)	MAE (%)	R	C_V of SM
Dataset 1	29. 72	2.84	2.31	0.80	0.16
Dataset 2	30. 36	2.65	2.11	0.74	0.13
Dataset 3	7.46	2.77	2.10	0.92	0.94
Datasets 1 & 2	30.01	3.23	2.46	0.68	0.14
Datasets 2 & 3	19.18	4.05	2.70	0.95	0.66
Datasets 1 & 3	19.75	9.76	7.09	0.63	0.63
Datasets 1 & 2 & 3	23.14	8.26	5.70	0.71	0.50

From the results (see Table 3), we observed that the different test areas in this study area indicated different soil moisture content. This is because of the condition of the soil which might be plowed, unplowed, or irrigated. When we analyze Dataset 1 results; the average soil moisture of Dataset 1 was high at 29.72% and the Cv value of the ground soil moistures (SM) was around 0.16. Moreover, the soil surface was sparsely vegetated in this growth stage. This means that the data forming Dataset 1 were not uniformly distributed over the study area due to low vegetation. Therefore, the scattering parameters in Dataset 1 displayed a good R value, with slightly high error rates compared to other datasets.

Similarly, the average soil moisture value for Dataset 2 was near that of Dataset 1. Among the datasets, the lowest correlation coefficient $R = 0.706$ with the smallest estimation error was observed in this stage. The reason for the low R might be that the study area was densely vegetated on this date. Thus, the vegetation scattering decreased the correlation between the estimated and measured soil moisture. Furthermore, uniform data distribution was observed for Dataset 2 because of the dense vegetation impact, which caused low error rates at this stage.

In contrast to other datasets, the average soil moisture for Dataset 3 was low around 7%, which means that the surface was dry. However, a strong relationship between the measured and estimated soil moisture was established with the highest correlation coefficient: $R = 0.919$. This might be because the study area was bare in this growth stage, with high C_V of SM, and Dataset 3 was not distributed uniformly over the study area. Here, partial irrigation might impact the distribution of the soil moisture and increase the C_V of SM and R values.

By the time we considered all dataset combinations, the best estimation model was observed in Datasets 1 & 2 approach, with the smallest error rate. The reason for this might be that the C_V of SM for both Datasets 1 and 2 is low and the data distribution of the Dataset 2 was uniform. Moreover, the variation of ground soil moisture for Datasets 1 and 2 is restricted, with high soil moisture values around saturation. For this reason, error could be limited due to the saturation of the radar signal for these levels [34].

However, the worst estimation models were examined in Datasets 1 & 3 and Datasets 1 & 2 & 3 approaches. This might be because of that the distribution of Datasets 1 & 3 was not uniform and the soil moisture vertical profile for Dataset 3 was heterogeneous. Thus, Datasets 1 and 3 induced high error rates when combined with other datasets [35]. Furthermore, the roughness effect, which is an important parameter on bare soil conditions (Dataset 3), could generate significant error in soil moisture estimation [34].

The main contribution of the proposed system is that the datasets were constituted in a novel approach by combining the decomposed model parameters with the standard sigma backscattering coefficients. Then, the GRNN neural network was fed into by these parameters and estimated the soil moisture with a low error rate. Considering the literature studies, some of the main approaches for soil moisture estimation via SAR-based data are listed in Table 4. The overall accuracy of the proposed system indicated good results compared to the other approaches in the literature.

Table 4. The comparison of different approaches for estimating soil moisture by SAR-based data.

Reference	Province	Dataset	Accuracy	Methods
Proposed method	Bare & Vegetated fields (Turkey)	Radarsat-2 data & Ground measurements	R = [0.74–0.92] for each dataset R = [0.63–0.95] for combined datasets	Polarimetric Decomposition & GRNN
[2]	Vegetated fields (Germany)	POLSAR data & Ground measurements	R^2 = [0.4–0.7]	Polarimetric Decomposition
[4]	Bare fields: (China)	Radarsat-2,TerraSAR-X data & Ground measurements	R^2 = [0.82–0.86]	SVR & Modified Dubois
[6]	Bare & Vegetated fields (China)	Radarsat-2, Optical data & Ground measurements	R^2 = 0.71	IEM & WCM
[9]	Vegetated fields (Canada)	Radarsat-2 data & Ground measurements	RMSE = 7.12%	Adaptive Two Component Decomposition
[10]	Vegetated fields (China)	Radarsat-2 data & Ground measurements	R = 0.84	Advanced IEM
[21]	Bare and Lightly Vegetated fields (Italy)	ENVISAT/ASAR data & Ground measurements	R^2 = 0.82 all dataset R^2 = [0.45–0. 65] for single day data set.	IEM, ANN, Bayesian & Nelder–Mead
[36]	Vegetated fields (Canada)	UAVSAR data & Ground measurements	R = [non–0.66]	Simplified Polarimetric Decomposition
[37]	Farmland (China)	Radarsat-2 data & Ground measurements	R^2 = 0.41	Improved WCM
[38]	Vegetated fields (China)	Radarsat-2 data & Ground measurements	R^2 = [0.83–0.88]	Polarimetric Decomposition, Bragg, X-Bragg & ISSM
[39]	Vegetated fields (USA)	Radarsat-1, Landsat data & Ground measurements	R^2 = [0.72–0.76]	ANN, Fuzzy & Multivariate Statistics
[40]	Bare fields: (France)	Radarsat-2 data & Ground measurements	RMSE = [0.06–0.09] cm^3/cm^3	MLP & IEM

6. Conclusions

In this paper, polarimetric decomposition models with the aid of standard sigma backscattering coefficients were implemented to form feature vectors. The GRNN algorithm was then used to estimate the regional soil moisture content on the basis of multi-band Radarsat-2 data. Eventually, the proposed system gave good results for single C-band SAR data over the study area and these results showed that radar is an appropriate remote sensing tool for the retrieval of surface soil moisture with very low mean absolute error over the study area. However, the validation of all results was restricted due to a lack of ground measurements for vegetation and roughness parameters.

In the future, we are planning to acquire different SAR-based data and ground measurements to improve the accuracy of the proposed system with an increasing number of datasets. Moreover, the adaptability of different feature extraction methods will be examined for the soil moisture estimation model. Since this study is a joint project of TARBIL (Agricultural Monitoring and Information System) and TUBİTAK (The Scientific and Technological Research Council of Turkey), it is thought that improving the estimation model will allow for classifying agricultural land into two groups: dry and wet soil. Thus, natural water resources can be used more efficiently and the optimum water amount can be automatically determined for irrigation purposes in this region.

Acknowledgments: The authors wish to thank the ESA for providing the Sentinel-I software. This study was supported by a research project of TUBITAK (No. 114E543), Dicle University Scientific Research Projects (DUBAP) Unit, and a TARBIL project.

Author Contributions: Mehmet Siraç Özerdem and Remzi Ekinci designed the research; Emrullah Acar, Remzi Ekinci, and Mehmet Siraç Özerdem contributed ground measurements; Emrullah Acar performed the software analysis; Emrullah Acar, Remzi Ekinci, and Mehmet Siraç Özerdem analyzed the data; Remzi Ekinci and Mehmet Siraç Özerdem contributed materials and analysis tools; Emrullah Acar and Mehmet Siraç Özerdem wrote the paper.

Conflicts of Interest: The authors declare no conflict of interest.

References

1. Idso, S.B.; Jackson, R.D.; Reginato, R.J. Detection of soil moisture by remote surveillance. *Am. Sci.* **1975**, *63*, 549–557.
2. Hajnsek, I.; Jagdhuber, T.; Schon, H.; Papathanassiou, K.P. Potential of estimating soil moisture under vegetation cover by means of PolSAR. *IEEE Trans. Geosci. Remote Sens.* **2009**, *47*, 442–454. [CrossRef]
3. Gorrab, A.; Zribi, M.; Baghdadi, N.; Mougenot, B.; Fanise, P.; Chabaane, Z.L. Retrieval of both soil moisture and texture using TerraSAR-X images. *Remote Sens.* **2015**, *7*, 10098–10116. [CrossRef]
4. Zhang, X.; Chen, B.; Fan, H.; Huang, J.; Zhao, H. The Potential Use of Multi-Band SAR Data for Soil Moisture Retrieval over Bare Agricultural Areas: Hebei, China. *Remote Sens.* **2016**, *8*, 7. [CrossRef]
5. Oliver, C.; Quegan, S. *Understanding Synthetic Aperture Radar Images*; SciTech Publishing: Stevenage, UK, 2004.
6. He, B.; Xing, M.; Bai, X. A Synergistic methodology for soil moisture estimation in an alpine prairie using radar and optical satellite data. *Remote Sens.* **2014**, *6*, 10966–10985. [CrossRef]
7. Yang, J.; Yamaguchi, Y.; Lee, J.S.; Touzi, R.; Boerner, W.M. Applications of Polarimetric SAR. *J. Sens.* **2015**, *316391*, 1–3. [CrossRef]
8. Jagdhuber, T.; Hajnsek, I.; Bronstert, A.; Papathanassiou, K.P. Soil Moisture Estimation Under low vegetation cover using a multi-angular polarimetric decomposition. *IEEE Trans. Geosci. Remote Sens.* **2013**, *51*, 2201–2215. [CrossRef]
9. Xiaodong, H.; Jinfei, W.; Jiali, S. Adaptive Two-Component Model-Based Decomposition on Soil Moisture Estimation for C-Band RADARSAT-2 Imagery over Wheat Fields at Early Growing Stages. *IEEE Geosci. Remote Sens. Lett.* **2016**, *13*, 414–418.
10. Bai, X.; He, B.; Li, X. Optimum surface roughness to parameterize advanced integral equation model for soil moisture retrieval in prairie area using Radarsat-2 data. *IEEE Trans. Geosci. Remote Sens.* **2016**, *5*, 2437–2449. [CrossRef]
11. Hajnsek, I.; Cloude, S.R.; Lee, J.S.; Pottier, E. Inversion of surface parameters from polarimetric SAR data. In Proceedings of the IEEE International Geoscience and Remote Sensing Symposium, Honolulu, HI, USA, 24–28 July 2000; pp. 1095–1097.
12. Oh, Y.; Sarabandi, K.; Ulaby, F.T. An empirical model and an inversion technique for radar scattering from bare soil surfaces. *IEEE Trans. Geosci. Remote Sens.* **1992**, *30*, 370–381. [CrossRef]
13. Dubois, P.C.; Van Zyl, J.J.; Engman, E.T. Measuring soil moisture with imaging radars. *IEEE Trans. Geosci. Remote Sens.* **1995**, *33*, 915–926. [CrossRef]
14. Oh, Y. Semi-empirical model of the ensemble-averaged differential Mueller matrix for microwave backscattering from bare soil surfaces. *IEEE Trans. Geosci. Remote Sens.* **2002**, *40*, 1348–1355. [CrossRef]
15. Fung, A.K.; Chen, K.S. An update on the IEM surface backscattering model. *IEEE Geosci. Remote Sens. Lett.* **2004**, *1*, 75–77. [CrossRef]
16. Notarnicola, C.; Angiulli, M.; Posa, F. Soil moisture retrieval from remotely sensed data: Neural network approach versus Bayesian method. *IEEE Trans. Geosci. Remote Sens.* **2008**, *46*, 547–557. [CrossRef]
17. Said, S.; Kothyari, U.C.; Arora, M.K. ANN-based soil moisture retrieval over bare and vegetated areas using ERS-2 SAR data. *J. Hydrol. Eng.* **2008**, *13*, 461–475. [CrossRef]
18. Pasolli, L.; Notarnicola, C.; Bruzzone, L. Estimating soil moisture with the support vector regression technique. *IEEE Geosci. Remote Sens. Lett.* **2011**, *8*, 1080–1084. [CrossRef]
19. Pasolli, L.; Notarnicola, C.; Bruzzone, L.; Bertoldi, G.; Chiesa, S.D.; Niedrist, G.; Tappeiner, U.; Zebisch, M. Polarimetric RADARSAT-2 imagery for soil moisture retrieval in alpine areas. *Can. J. Remote Sens.* **2011**, *37*, 535–547. [CrossRef]
20. Ahmad, S.; Kalra, A.; Stephen, H. Estimating soil moisture using remote sensing data: A machine learning approach. *Adv. Water Resour.* **2010**, *33*, 69–80. [CrossRef]

21. Paloscia, S.; Pampaloni, P.; Pettinato, S.; Santi, E. A comparison of algorithms for retrieving soil moisture from ENVISAT/ASAR images. *IEEE Trans. Geosci. Remote Sens.* **2008**, *46*, 3274–3284. [CrossRef]
22. Weimann, A. Inverting a microwave backscattering model by the use of a neural network for the estimation of soil moisture. In Proceedings of the IEEE International Geoscience and Remote Sensing Symposium, Seattle, WA, USA, 6–10 July 1998; pp. 1837–1839.
23. Xie, X.M.; Xu, J.W.; Zhao, J.F.; Liu, S.; Wang, P. Soil moisture inversion using AMSR-E remote sensing data: An artificial neural network approach. *Appl. Mech. Mater.* **2014**, *501–504*, 2073–2076. [CrossRef]
24. Srivastava, P.K.; Han, D.; Ramirez, M.R.; Islam, T. Machine learning techniques for downscaling SMOS satellite soil moisture using MODIS land surface temperature for hydrological application. *Water Resour. Manag.* **2013**, *27*, 3127–3144. [CrossRef]
25. Prasad, R.; Kumar, R.; Singh, D. A radial basis function approach to retrieve soil moistrure and crop variables from Xband scatterometer ovservations. *Prog. Electromagn. Res. B* **2009**, *12*, 201–217. [CrossRef]
26. Bourgeau-Chavez, L.L.; Leblon, B.; Charbonneau, F.; Buckley, J.R. Evaluation of polarimetric Radarsat-2 SAR data for development of soil moisture retrieval algorithms over a chronosequence of black spruce boreal forests. *Remote Sens. Environ.* **2013**, *132*, 71–85. [CrossRef]
27. Charbonneau, F. Using RADARSAT-2 polarimetric and ENVISAT-ASAR dual-polarization data for estimating soil moisture over agricultural fields. *Can. J. Remote Sens.* **2012**, *38*, 514–527.
28. European Space Agency (ESA). Available online: https://earth.esa.int (accessed on 13 February 2017).
29. Freeman, A.; Durden, S.L. A three component scattering model for polarimetric SAR data. *IEEE Trans. Geosci. Remote Sens.* **1998**, *36*, 963–973. [CrossRef]
30. Cloude, S.R.; Pottier, E. An entropy based classification scheme for land applications of polarimetric SAR. *IEEE Trans. Geosci. Remote Sens.* **1997**, *35*, 68–78. [CrossRef]
31. Specht, D.F. A general regression neural network. *IEEE Trans. Neural Netw.* **1991**, *2*, 568–576. [CrossRef] [PubMed]
32. Ali, I.; Greifeneder, F.; Stamenkovic, J.; Neumann, M.; Notarnicola, C. Review of Machine Learning Approaches for Biomass and Soil Moisture Retrievals from Remote Sensing Data. *Remote Sens.* **2015**, *7*, 16398–16421. [CrossRef]
33. Li, W.; Yang, X.; Li, H.; Su, L. Hybrid Forecasting Approach Based on GRNN Neural Network and SVR Machine for Electricity Demand Forecasting. *Energies* **2017**, *10*, 44. [CrossRef]
34. Zribi, M.; Baghdadi, N.; Holah, N.; Fafin, O.; Guérin, C. Evaluation of a rough soil surface description with ASAR-ENVISAT Radar Data. *Remote Sens. Environ.* **2005**, *95*, 67–76. [CrossRef]
35. Le Morvan, A.; Zribi, M.; Baghdadi, N.; Chanzy, A. Soil Moisture Profile Effect on Radar Signal Measurement. *Sensors* **2008**, *8*, 256–270. [CrossRef] [PubMed]
36. Wang, H.; Magagi, R.; Goita, K.; Jagdhuber, T.; Hajnsek, I. Evaluation of Simplified Polarimetric Decomposition for Soil Moisture Retrieval over Vegetated Agricultural Fields. *Remote Sens.* **2016**, *8*, 142. [CrossRef]
37. Yang, G.; Yue, J.; Li, C.; Feng, H.; Yang, H.; Lan, Y. Estimation of soil moisture in farmland using improved water cloud model and Radarsat-2 data. *Trans. Chin. Soc. Agric. Eng.* **2016**, *32*, 146–153.
38. Xie, Q.; Meng, Q.; Zhang, L.; Wang, C.; Sun, Y.; Sun, Z. A Soil Moisture Retrieval Method Based on Typical Polarization Decomposition Techniques for a Maize Field from Full-Polarization Radarsat-2 Data. *Remote Sens.* **2017**, *9*, 168. [CrossRef]
39. Lakhankar, T.; Ghedira, H.; Temimi, M.; Sengupta, M.; Khanbilvardi, R.; Blake, R. Non-Parametric methods for soil moisture retrieval from satellite remote sensing data. *Remote Sens.* **2009**, *1*, 3–21. [CrossRef]
40. Baghdadi, N.; Cresson, R.; El Hajj, M.; Ludwig, R.; La Jeunesse, I. Estimation of soil parameters over bare agriculture areas from C-band polarimetric SAR data using neural networks. *Hydrol. Earth Syst. Sci.* **2012**, *16*, 1607–1621. [CrossRef]